IOP PUBLISHING JOURNAL OF PHYSICS D: APPLIED PHYSICS

J. Phys. D: Appl. Phys. **40** (2007) 2476–2490 doi:10.1088/0022-3727/40/8/010

H_2 generation in Ar/NH_3 microdischarges

Ramesh A Arakoni[1], Ananth N Bhoj[2,5] and Mark J Kushner[3,4]

[1] Department of Aerospace Engineering, University of Illinois at Urbana-Champaign, Urbana, IL 61801, USA
[2] Department of Chemical and Biomolecular Engineering, University of Illinois at Urbana-Champaign, Urbana, IL 61801, USA
[3] Department of Electrical and Computer Engineering, Iowa State University, Ames, IA 50011, USA

E-mail: arakoni@uiuc.edu, ananth.bhoj@novellus.com and mjk@iastate.edu

Received 2 December 2006, in final form 20 February 2007
Published 4 April 2007
Online at stacks.iop.org/JPhysD/40/2476

Abstract
Due to the difficulty of H_2 storage, development of real time H_2 generators would be advantageous for portable fuel cells. In this paper, the real time production of H_2 using microdischarge devices is discussed with results from a computational investigation. Ar/NH_3 mixtures were studied using plug flow and two-dimensional models. Dissociation of NH_3 by electron impact and thermal processes produces H atoms which recombine to form H_2. We found that for sandwich type microdischarges with a diameter of 300 μm, dissociation of NH_3 is approximately 95% by electron impact and 5% by thermal processes for a NH_3 mole fraction of 5%. Efficiency of conversion of NH_3 to H_2 is dependent on residence time in the discharge, mole fraction and geometry, as these properties determine the eV/molecule deposited into NH_3. Conversion efficiencies (fraction of H in NH_3 converted to H_2) in excess of 83% are predicted for optimum conditions.

1. Introduction

Fuel cells based on H_2 are gaining importance as alternative energy sources due to the increasing cost of non-renewable sources of energy. They also address environmental concerns such as global warming as the effluent of their power production is water vapour. Advances in fuel cell technology have led to efficient (>50%) conversion of chemical ($H_2 + 1/2O_2 \rightarrow H_2O$; $\Delta H = -2.5$ eV) to electrical energy. [1]

Storage of H_2 for use in fuel cells is problematic as it liquefies only under extreme temperatures and pressure and its highly combustive nature requires caution. Thus, it is worth investigating methods of *in situ* production of molecular hydrogen for portable applications. In this paper, we discuss results from computational investigations of the use of Ar/NH_3 mixtures for production of H_2 in microdischarge devices. Although NH_3 is commercially produced by reactions between N_2 and H_2, it is also a by-product of natural biological processes and refineries. It has high H content (17% by mass), is easily liquefied and the end products are stable (N_2, H_2, some N_xH_y). Feedstock gases such as methane have higher H_2 content but they need to be partially oxidized to produce H_2 and the by-products include greenhouse gases such as CO_2.

NH_3 plasmas are used in various applications such as surface treatment to improve wettability and biocompatibility of polymer surfaces [2] and surface nitridation for semiconductor applications [3]. Van den Oever *et al* [4, 5] investigated the production of NH and NH_2 in expanding Ar/NH_3 plasmas for possible use in ultrahigh-rate deposition of Si_3N_4 films. Recent interest in NH_3 plasmas includes high pressure (0.1–1 atm) dielectric barrier discharges (DBDs) and micro-hollow cathode discharges for conversion of NH_3 to H_2. Experiments by Qiu *et al* [6] demonstrated a 20% conversion of H atoms in NH_3 to H_2 in atmospheric pressure microdischarges. Pulsing of the discharge improved the efficiency of conversion, as did using an array of microdischarges. Hsu and Graves [7] investigated the

[4] Author to whom any correspondence should be addressed.

[5] Present address: Novellus Systems, Inc., 3011 N. 1st St, San Jose, CA 95134 USA.

decomposition of ammonia in microdischarges at hundreds of torr at power levels of 1–5 W. They demonstrated a strong dependence of the conversion rate to hydrogen on the residence time (or flow rates) and used it as a means to vary the eV/NH_3-molecule. They also showed that thermal as well as electron impact dissociation could be important in the conversion process. By fitting their data to a plug flow model, they predicted the gas temperature to be as high as 2000 K. Fateev *et al* [8] investigated Ar/NH_3 plasma chemistry in a DBD and modelled the chemical kinetics. They observed that the discharge produced stable species such as N_2, H_2 and N_2H_4. At power densities of 1.2 W cm^{-3}, they found that the leading source of NH_3 decomposition (to NH and NH_2) was collisions of NH_3 with Ar metastables.

Miller and Baird [9] studied the decomposition of NH_3 in radio frequency plasmas at pressures of a few to 40 Torr. They found the conversion of NH_3 to H_2 to be between 4.2 and 30 molecules/100 eV of deposited energy in inductively coupled plasmas, a value higher than that observed in capacitively coupled plasmas. At pressures above 20 Torr, they were unable to completely dissociate the NH_3.

In this paper, we discuss results from a computational investigation of the use of microdischarges sustained in Ar/NH_3 mixtures for real time generation of H_2. These investigations were performed using plug flow (quasi-one dimensional) and two-dimensional models. The plug flow model was useful to investigate scaling laws over a large parameter space. The 2D model was used to address flow issues, the non-equilibrium nature of the discharge near the cathode and the spatial variation of the plasma characteristics such as power density, electron temperature and plasma potential.

We found that the efficiency of H production by electron impact dissociation of NH_3 is a sensitive function of electron temperature (T_e), optimizing at 3 eV or less depending on gas mixture. H_2 densities of 10^{16} cm^{-3} can be obtained with power densities of 2.5 kW cm^{-3} and an NH_3 mole fraction of 0.1 at 100 Torr. The hydrogen conversion efficiency, η, is the fraction of H atoms entering the discharge as NH_3 and exiting the discharge as H_2. For a given power deposition, we found that η increased with increasing residence time and decreased with increasing mole fraction of NH_3. The conditions for high η are usually associated with a larger energy deposition per NH_3 molecule and usually, a higher energy deposition per H_2 molecule exiting the discharge, $\gamma(H_2)$. Values of η as high as 0.9 are predicted based on results from the plug flow model. A higher η implies a better utilization of the incoming feedstock gas (NH_3) and a lower $\gamma(H_2)$ implies an efficient utilization of the power deposited in the plasma. These two factors will ultimately determine whether this process could be practically used to locally generate H_2 for technological purposes. As such, this paper will focus on ways to produce H_2 with high η, efficient utilization of NH_3, and low $\gamma(H_2)$, greater power efficiency.

The models used in this investigation are described in section 2 and followed by a description of the Ar/NH_3 reaction chemistry in section 3. The results from the modelling are discussed in sections 4 and 5, followed by our concluding remarks in section 6.

2. Description of the models

The plug flow model used in this study, GlobalKIN, has been previously described in [10, 11] and so will be only briefly discussed here. GlobalKIN is a volume averaged, global kinetics model for plasma chemistry which, in plug flow mode, resolves axial transport. GlobalKIN consists of a plasma chemistry module, a surface kinetics module and an electron energy transport module. The plasma chemistry module provides the time rate of change of species based on gas-phase chemistry and surface reactions. T_e and average gas temperature, T_g, are also solved for by integrating their respective conservation equations. Assuming a linear axial flow, transport to radial surfaces is included by using a diffusion length. The surface kinetics module employs a surface site-balance model which provides surface reaction coefficients used in the volumetric model. The electron energy transport module consists of a solution to Boltzmann's equation for the electron energy distribution (EED) which provides electron impact rate coefficients based on the EEDs and fundamental cross-sections. The resulting rate equations are integrated in time using a stiff ordinary differential equation solver. By simultaneously calculating the axial speed of the flow based on constant pressure, change in enthalpy, species densities and gas temperature, the integration in time is mapped to axial position.

NonPDPSIM was used to investigate flow and transport issues of NH_3 microdischarges. nonPDPSIM is described in detail in [12–14] and so will be only briefly discussed here. nonPDPSIM is a two-dimensional plasma hydrodynamics model that accounts for the reaction chemistry and flow dynamics. Continuity equations for charged gas-phase species, surface charges and Poisson's equation for the electric potential are simultaneously implicitly integrated in time using a sparse matrix technique. Updates of these quantities are followed, in a time splicing manner, with updates of T_e and neutral fluid quantities. The latter includes individual species densities by integrating continuity equations and bulk fluid mass density, momentum and temperature through integration of the compressible Navier–Stokes equations. Monte Carlo algorithms are used to track the trajectories of secondary electrons emitted from the cathode. Momentum transfer from charged species to neutral species was also included. A simple circuit model was used to interface the plasma with metal surfaces connected to a voltage source and circuit elements (e.g. ballast resistor). The current flowing into the metal surfaces and the impedance of the circuit, are used to determine the voltages on the metal surfaces. The power supply voltages were adjusted to deposit the specified power in the plasma.

A schematic of the reactor used in this investigation is shown in figure 1(*a*). The discharge region is 300 μm in diameter. The electrodes are 250 μm thick and their centres are separated by a 1 mm thick dielectric. The cathode is downstream and powered, whereas the anode (upstream) is grounded. The inlet and outlet boundaries are sufficiently far away ((5–10) $\times$ diameter of the plasma) so that the bulk plasma properties would not be affected by the artificial boundaries.

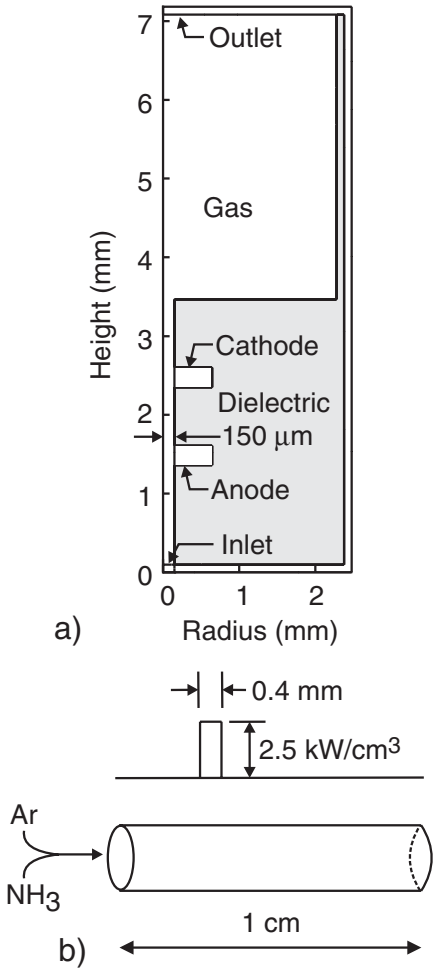

Figure 1. Geometry of the reactors: (*a*) structure of the cylindrically symmetric discharge used for the 2D model and (*b*) schematic of plug flow model.

3. Reaction mechanism

The reaction mechanism for the plasma chemistry of Ar/NH_3 mixtures is listed in table 1. The species included in the mechanism are: e, Ar, Ar(4s) (referred to as Ar^*), Ar(4p) (referred to as Ar^{**}), Ar_2^*, Ar^+, Ar_2^+, ArH^+, NH_3, NH_3^+, NH_4^+, $NH_3(v)$, NH_2, NH_2^+, NH_2^-, NH, NH^+, N, N^+, N_2, H, H^+, H^-, H_2, H_2^+, H_3^+, N_2H_2, N_2H_3 and N_2H_4.

The Ar plasma chemistry used in the model has been discussed in [15] in the context of high pressure discharges in lamps. In this section we discuss the Ar/NH_3 chemistry with an emphasis on the H and H_2 production mechanisms. The primary source of H production in the discharge is by electron impact dissociation of NH_3,

$$e + NH_3 \rightarrow NH_2 + H + e(\Delta\varepsilon = 5.6\,eV), \qquad (1a)$$

$$e + NH_3 \rightarrow NH + H + H + e(\Delta\varepsilon = 8.9\,eV), \qquad (1b)$$

where $\Delta\varepsilon$ is the threshold energy. Ar^*, Ar^{**} and Ar^+, with energies of 11.6, 13.1 and 16 eV, respectively, have enough energy to charge-exchange or Penning ionize and so dissociate NH_3,

$$Ar^{*,**} + NH_3 \rightarrow NH_3^+ + Ar + e \quad (k = 4.2 \times 10^{-11}\,cm^3\,s^{-1}), \qquad (2a)$$

$$\rightarrow NH_2 + H + Ar \quad (k = 5.8 \times 10^{-11}\,cm^3\,s^{-1}), \qquad (2b)$$

$$\rightarrow NH + H + H + Ar \quad (k = 5.2 \times 10^{-11}\,cm^3 s^{-1}), \qquad (2c)$$

$$Ar^+ + NH_3 \rightarrow NH_3^+ + Ar \quad (k = 1.3 \times 10^{-9}\,cm^3\,s^{-1}), \qquad (2d)$$

$$NH_2^+ + H + Ar \quad (k = 5.5 \times 10^{-11}\,cm^3 s^{-1}), \qquad (2e)$$

where k is the rate coefficient at room temperature unless noted otherwise. The branching ratio of equation (2*d*) to form ArH^+ and NH_2 is small (< 3%) and so the presence of ArH^+ is not a major factor in the production of H_2. This is mainly because dissociative recombination and other charge exchange reactions can quickly consume the ArH^+, releasing the H back into the discharge. The results discussed here from the plug flow model include the ArH^+ in the reaction mechanism. Test cases were run using the plug flow model with and without ArH^+ in the mechanism. The results yielded H_2 densities that were within 0.3% of each other. Based on the insensitivity of the reaction mechanism to the presence of ArH^+ and the need to speed the more extensive 2D calculations, ArH^+ was excluded from the 2D investigation.

Charge exchange between Ar^+, and NH, NH_2 and NH_3 species produces the respective NH_x^+ ions. Further charge exchange between NH_x^+ ions leads to the formation of NH_4^+, which has the smallest ionization potential among all the ions in the mechanism:

$$NH_3^+ + NH_3 \rightarrow NH_4^+ + NH_2 \qquad (k = 2.2 \times 10^{-9}\,cm^3\,s^{-1}). \qquad (3)$$

As such, the density of NH_4^+ tends to be large if NH_x species are not significantly depleted. Dissociative recombination of NH_x^+ produces NH_{x-1} and H as the dominant channels. These reactions also produce thermal energy by Franck–Condon heating, whereby potential energy in the dissociative electronic states is converted to translational energy and contributes to the change in enthalpy, ΔH, of the gas mixture,

$$e + NH_4^+ \rightarrow NH_3 + H \quad (k = 9.0 \times 10^{-7} T_e^{-0.6}\,cm^3\,s^{-1},\ \Delta H = -4.7\,eV), \qquad (4a)$$

$$\rightarrow NH_2 + H + H \quad (k = 1.5 \times 10^{-7} T_e^{-0.6}\,cm^3\,s^{-1},\ \Delta H = -0.3\,eV), \qquad (4b)$$

where the electron temperature T_e is in eV.

The gas temperature can increase by many hundreds of kelvin to reach over 1000 K [7] while flowing through the discharge and so thermal dissociation processes can also contribute significantly to H production. For example, although the thermal dissociation of NH_3 by argon,

$$NH_3 + Ar \rightarrow H_2 + NH + Ar \quad (k = 6.1 \times 10^{-20}\,cm^3\,s^{-1}\ \text{at}\ 2000\,K), \qquad (5)$$

Table 1. Ar/NH_3 reaction mechanism.

Species		
e	NH_3	NH_4^+
Ar	$NH_3(v)$	NH_3^+
Ar*(4s)	NH_2	NH_2^+
Ar**(4p)	NH	NH^+
Ar_2^*	N	N^+
Ar^+	N_2	H_3^+
Ar_2^+	N_2H_2	H_2^+
ArH^+	N_2H_3	H^+
	N_2H_4	NH_2^-
	H	H^-
	H_2	

Reaction	Rate coefficient[a]	Reference
$e + Ar \rightarrow Ar + e$	[b]	[18]
$e + Ar \leftrightarrow Ar^* + e$	[b]	[19][c]
$e + Ar \leftrightarrow Ar^{**} + e$	[b]	[19][c]
$e + Ar \rightarrow Ar^+ + e + e$	[b]	[20]
$e + Ar^* \leftrightarrow Ar^{**} + e$	[b]	[21][c]
$e + Ar^* \rightarrow Ar^+ + e + e$	[b]	[22]
$e + Ar^{**} \rightarrow Ar^+ + e + e$	[b]	[23]
$e + Ar_2^* \rightarrow Ar_2^+ + e + e$	$9 \times 10^{-8}\ T_e^{0.7}\ e^{-3.66/T_e}$	[24]
$e + Ar_2^* \rightarrow Ar + Ar + e$	1×10^{-7}	[24]
$e + Ar_2^+ \rightarrow Ar^{**} + Ar$	$5.4 \times 10^{-8} T_e^{-0.66}$	[24]
$e + Ar^+ \rightarrow Ar^{**}$	$4 \times 10^{-13} T_e^{-0.5}$	[25]
$e + e + Ar^+ \rightarrow Ar^{**} + e$	$5 \times 10^{-27} T_e^{-4.5}$	[25]
$e + NH_3 \rightarrow NH_3 + e$	[b]	[26]
$e + NH_3 \leftrightarrow NH_3(v) + e$	[b]	[26][c]
$e + NH_3 \rightarrow NH_2 + H^-$	[b]	[26]
$e + NH_3 \rightarrow NH_2 + H + e$	[b]	[26]
$e + NH_3 \rightarrow NH + H + H + e$	[b]	[26]
$e + NH_3 \rightarrow NH_3^+ + e + e$	[b]	[26]
$e + NH_3 \rightarrow NH_2^+ + H + e + e$	[b]	[27]
$e + NH_3(v) \rightarrow NH_3(v) + e$	[b]	[26]
$e + NH_3(v) \rightarrow NH_2 + H^-$	[b]	[26][d]
$e + NH_3(v) \rightarrow NH_2 + H + e$	[b]	[26][e]
$e + NH_3(v) \rightarrow NH + H + H + e$	[b]	[26][e]
$e + NH_3(v) \rightarrow NH_3^+ + e + e$	[b]	[27][e]
$e + NH_3(v) \rightarrow NH_2^+ + H + e + e$	[b]	[27][e]
$e + NH_2 \rightarrow NH_2 + e$	[b]	[26][f]
$e + NH_2 \rightarrow NH + H^-$	[b]	[26]
$e + NH_2 \rightarrow NH + H + e$	[b]	[26]
$e + NH_2 \rightarrow N + H + H + e$	[b]	[28]
$e + NH_2 \rightarrow NH_2^+ + e + e$	[b]	[28]
$e + NH_2 \rightarrow NH^+ + H + e + e$	[b]	[28]
$e + NH \rightarrow NH + e$	[b]	[26][f]
$e + NH \rightarrow N + H + e$	[b]	[26]
$e + NH \rightarrow N^+ + H + e + e$	[b]	[28]
$e + NH \rightarrow NH^+ + e + e$	[b]	[28]
$e + N \rightarrow N + e$	[b]	[29]
$e + N \rightarrow e + N^*$	[b,g]	[30]
$e + N \rightarrow N^+ + e + e$	[b]	[31]
$e + N_2 \rightarrow N_2 + e$	[b]	[32]
$e + N_2 \rightarrow N_2(v) + e$	[b,g]	[32]
$e + N_2 \rightarrow N_2^* + e$	[b,g]	[32]
$e + N_2 \rightarrow N + N + e$	[b]	[33]
$e + N_2 \rightarrow N_2^+ + e + e$	[b]	[32]
$e + H \rightarrow H + e$	[b]	[34]
$e + H \rightarrow H^* + e$	[b,g]	[35]
$e + H \rightarrow H^+ + e + e$	[b]	[35]
$e + H_2 \rightarrow H_2 + e$	[b]	[36]
$e + H_2 \rightarrow H_2(v) + e$	[b,g]	[36]
$e + H_2 \rightarrow H_2^* + e$	[b,g]	[36]
$e + H_2 \rightarrow H_2^+ + e + e$	[b]	[36]
$e + H_2 \rightarrow H + H + e$	[b]	[37]
$e + H^+ \rightarrow H$	$4 \times 10^{-13} T_e^{-0.5}$	[25]

Table 1. (continued)

Reaction	Rate coefficient	Reference
$e + H_2^+ \rightarrow H^+ + H + e$	[b]	[38]
$e + H_2^+ \rightarrow H + H$	$1 \times 10^{-7} T_e^{-0.4}$	[39]
$e + H_3^+ \rightarrow H^+ + H_2$	[b]	[38]
$e + H_3^+ \rightarrow H + H_2$	[b]	[40]
$e + ArH^+ \rightarrow Ar + H$	[b]	[40]
$e + N^+ \rightarrow N$	$4 \times 10^{-13} T_e^{-0.5}$	[25]
$e + NH^+ \rightarrow N + H$	$1 \times 10^{-7} T_e^{-0.5}$	[40]
$e + NH_2^+ \rightarrow NH + H$	$1 \times 10^{-7} T_e^{-0.5}$	[40]
$e + NH_3^+ \rightarrow NH_2 + H$	$1 \times 10^{-7} T_e^{-0.5}$	[40]
$e + NH_4^+ \rightarrow NH_3 + H$	$9 \times 10^{-7} T_e^{-0.6}$	[41]
$e + M^+ \rightarrow M^+ + e$	[b]	[42]
$Ar^+ + Ar \rightarrow Ar + Ar^+$	4.6×10^{-10}	[43]
$Ar^+ + Ar + M \rightarrow Ar_2^+ + M$	2.5×10^{-31}	[24][h,i]
$Ar^+ + NH_3, NH_3(v) \rightarrow NH_2^+ + H + Ar$	5.5×10^{-11}	[44]
$Ar^+ + M \rightarrow Ar + M^+$	1.3×10^{-9}	[44][j]
$Ar^+ + NH_3, NH_3(v) \rightarrow ArH^+ + NH_2$	9.2×10^{-11}	[44]
$Ar^+ + NH_2 \rightarrow NH^+ + H + Ar$	5.5×10^{-11}	[44][h]
$Ar^+ + H_2 \rightarrow H_2^+ + Ar$	1×10^{-9}	[44]
$Ar^+ + H_2 \rightarrow H^+ + H + Ar$	1×10^{-9}	[44]
$Ar^+ + H_2 \rightarrow ArH^+ + H$	1×10^{-9}	[44]
$Ar^+ + N \rightarrow N^+ + Ar$	1×10^{-11}	[44]
$Ar^+ + N_2 \rightarrow N^+ + N + Ar$	5×10^{-12}	[44][h]
$Ar^+ + H \rightarrow H^+ + Ar$	1×10^{-10}	[44]
$H_2^+ + N \rightarrow N^+ + H_2$	5×10^{-10}	[44][h]
$H_2^+ + H \rightarrow H^+ + H_2$	6.4×10^{-10}	[44]
$H_2^+ + H_2 \rightarrow H_3^+ + H$	2.1×10^{-9}	[44]
$H_2^+ + M \rightarrow H_2 + M^+$	5×10^{-10}	[44][h,j]
$H_2^+ + NH_x \rightarrow NH_{x+1}^+ + H\ (x = 1, 2, 3)$	5×10^{-11}	[44][h]
$N^+ + H \rightarrow N + H^+$	2×10^{-9}	[44][h]
$N^+ + H_2 \rightarrow NH^+ + H$	5.6×10^{-10}	[44]
$N^+ + M \rightarrow N + M^+$	2.4×10^{-9}	[44][h,j]
$Ar_2^+ + M \rightarrow Ar + Ar + M^+$	4.5×10^{-10}	[44][j]
$Ar_2^+ + H \rightarrow H^+ + Ar + Ar$	5×10^{-11}	[44][h]
$Ar_2^+ + H_2 \rightarrow ArH^+ + Ar + H$	4.7×10^{-10}	[44]
$H^+ + M \rightarrow H + M^+$	5×10^{-11}	[j,k]
$NH^+ + NH_3, NH_3(v) \rightarrow NH_3^+ + NH$	1.8×10^{-9}	[44]
$NH^+ + NH_3, NH_3(v) \rightarrow NH_4^+ + N$	6×10^{-10}	[44][h]
$NH^+ + NH_2 \rightarrow NH + NH_2^+$	1.8×10^{-9}	[44][k]
$NH^+ + H_2 \rightarrow NH_2^+ + H$	1×10^{-9}	[44]
$NH_2^+ + NH_3, NH_3(v) \rightarrow NH_3^+ + NH_2$	1.1×10^{-9}	[44][h]
$NH_2^+ + NH_3, NH_3(v) \rightarrow NH_4^+ + NH$	1.1×10^{-9}	[44][h]
$NH_2^+ + H_2 \rightarrow NH_3^+ + H$	1×10^{-9}	[44]
$ArH^+ + H_2 \rightarrow H_3^+ + Ar$	5×10^{-10}	[44]
$H_3^+ + NH_3 \rightarrow NH_4^+ + H_2$	4.4×10^{-9}	[44]
$NH_3^+ + NH_3, NH_3(v) \rightarrow NH_3^+ + NH_2$	2.0×10^{-10}	[44]
$NH_3^+ + NH_3, NH_3(v) \rightarrow NH_4^+ + NH_2$	2.2×10^{-9}	[44]
$NH_3^+ + H_2 \rightarrow NH_4^+ + H$	4×10^{-13}	[44]
$NH_2^- + H_2 \rightarrow H^- + NH_3$	2.3×10^{-11}	[44]
$H^- + H \rightarrow H_2 + e$	1.8×10^{-9}	[44]
$H^- + NH_3, NH_3(v) \rightarrow NH_2^- + H_2$	8.8×10^{-13}	[44]
$H^- + M^+ \rightarrow H + M$	3×10^{-6}	[k,l]
$H^- + M^+ \rightarrow H + M$	2×10^{-7}	[k,m]
$H^- + Ar_2^+ \rightarrow H + Ar + Ar$	2×10^{-7}	[k]
$H^- + ArH^+ \rightarrow Ar + H + H$	2×10^{-7}	[k]
$H^- + H_3^+ \rightarrow H_2 + H_2$	1×10^{-7}	[k]
$H^- + H_3^+ \rightarrow H_2 + H + H$	1×10^{-7}	[k]
$NH_2^- + M^+ \rightarrow NH_2 + M$	2×10^{-7}	[k,n]
$NH_2^- + NH_4^+ \rightarrow NH_2 + NH_3 + H$	2×10^{-7}	[k]
$NH_2^- + Ar_2^+ \rightarrow NH_2 + Ar + Ar$	2×10^{-7}	[k]
$NH_2^- + ArH^+ \rightarrow NH_3 + Ar$	1×10^{-7}	[k]
$NH_2^- + ArH^+ \rightarrow NH_2 + Ar + H$	1×10^{-7}	[k]
$NH_2^- + H_3^+ \rightarrow NH_3 + H_2$	1×10^{-7}	[k]
$NH_2^- + H_3^+ \rightarrow NH_2 + H_2 + H$	1×10^{-7}	[k]

Table 1. Continued

Reaction	Rate coefficient	Reference
$Ar^* + Ar^* \rightarrow Ar^+ + Ar + e$	1×10^{-9}	[24]
$Ar^* + Ar^{**} \rightarrow Ar^+ + Ar + e$	1×10^{-9}	[24]
$Ar^{**} + Ar^{**} \rightarrow Ar^+ + Ar + e$	1×10^{-9}	[24]
$Ar_2^* + Ar_2^* \rightarrow Ar_2^+ + Ar + Ar + e$	5×10^{-10}	[24]
$Ar^* + Ar + Ar \rightarrow Ar_2^* + Ar$	1.1×10^{-32}	[24]
$Ar^{**} + Ar + Ar \rightarrow Ar_2^* + Ar$	1.1×10^{-32}	[24]
$Ar_2^* \rightarrow Ar + Ar$	6×10^{7}	[24]
$Ar^{**} \rightarrow Ar^*$	2×10^{6}	[k]
$Ar^* \rightarrow Ar$	1×10^{1}	[45][o]
$Ar^{*,**} + NH_3, NH_3(v) \rightarrow Ar + NH_3^+ + e$	4.2×10^{-11}	[46]
$Ar^{*,**} + NH_3, NH_3(v) + H \rightarrow Ar + NH_2$	5.8×10^{-11}	[46]
$Ar^{*,**} + NH_3, NH_3(v) \rightarrow Ar + NH + 2H$	5.2×10^{-11}	[47]
$Ar^{*,**} + NH_3, NH_3(v) \rightarrow Ar + NH + H_2$	5.8×10^{-12}	[47]
$NH_3, NH_3(v) + Ar \rightarrow H_2 + NH + Ar$	$1.1 \times 10^{-9}\ e^{-47\,032/T_g}$	[48]
$N_2H_4 + Ar \rightarrow NH_2 + NH_2 + Ar$	$6.6 \times 10^{-9}\ e^{-20\,615/T_g}$	[49]
$NH_2 + Ar \rightarrow H + NH + Ar$	$2.2 \times 10^{-9}\ e^{-38\,224/T_g}$	[50]
$NH + Ar \rightarrow H + N + Ar$	$3 \times 10^{-10}\ e^{-37\,615/T_g}$	[50]
$N_2 + Ar \rightarrow N + N + Ar$	$4.3 \times 10^{-10}\ e^{-86\,460/T_g}$	[51]
$N_2 + N_2 \rightarrow N + N + N_2$	$4.3 \times 10^{-10}\ e^{-86\,460/T_g}$	[51]
$NH_3 + H \rightarrow H_2 + NH_2$	$6.5 \times 10^{-13}\ (T_g/300)^{2.76}\ e^{-5135/T_g}$	[52]
$NH_3(v) + H \rightarrow H_2 + NH_2$	$6.5 \times 10^{-13}\ (T_g/300)^{2.76} e^{-5135/T_g}$	[52]
$NH_2 + H \rightarrow NH + H_2$	$1.1 \times 10^{-10}\ e^{-4451/T_g}$	[53]
$NH_2 + H_2 \rightarrow H + NH_3$	$2.1 \times 10^{-12}\ e^{-4277/T_g}$	[46]
$NH_2 + NH_2 \rightarrow N_2H_2 + H_2$	1.3×10^{-12}	[54]
$NH_2 + NH_2 \rightarrow NH_3 + NH$	$1.8 \times 10^{-14}\ (T_g/300)^{2.79} e^{-660/T_g}$	[55]
$NH_2 + N \rightarrow N_2 + H + H$	1.2×10^{-10}	[46]
$NH_2 + NH \rightarrow N_2H_2 + H$	$2.5 \times 10^{-9}\ (T_g\ /300)^{-0.5}$	[46]
$NH_2 + NH \rightarrow N_2H_3$	1.2×10^{-10}	[56]
$NH + N \rightarrow N_2 + H$	2.5×10^{-11}	[57]
$NH + H \rightarrow H_2 + N$	$6 \times 10^{-11}\ e^{-166/T_g}$	[46]
$NH + NH \rightarrow N_2 + H + H$	1.2×10^{-9}	[58]
$NH + NH \rightarrow N_2H_2$	3.5×10^{-12}	[59]
$NH + NH \rightarrow NH_2 + N$	$1.4 \times 10^{-14}\ (T_g/300)^{2.89} e^{1015/T_g}$	[60]
$N + H_2 \rightarrow H + NH$	$2.7 \times 10^{-10}\ e^{-12\,609/T_g}$	[61]
$N_2H_2 + H \rightarrow N_2 + H_2 + H$	$4.5 \times 10^{-13}\ (T_g/300)^{2.63}\ e^{115/T_g}$	[62]
$H + H + M \rightarrow H_2 + M$	1.4×10^{-31}	[63][h,i]
$H + H + Ar \rightarrow H_2 + Ar$	$6.4 \times 10^{-33}\ (T_g/300)^{-1}$	[64]
$H + H + H_2 \rightarrow H_2 + H_2$	$8.9 \times 10^{-33}\ (T_g/300)^{-0.6}$	[64]
$H + H + H \rightarrow H_2 + H$	8.9×10^{-33}	[65]
$H + N + M \rightarrow NH + M$	5×10^{-32}	[46][h,i]
$H + NH_2 + M \rightarrow NH_3 + M$	6×10^{-30}	[46][h,i]
$H_2 + N + NH_3 \rightarrow NH_2 + NH_3$	1×10^{-36}	[66]
$N + N + Ar \rightarrow N_2 + Ar$	2.3×10^{-32}	[67]
$N + N + M \rightarrow N_2 + M$	7.2×10^{-33}	[68][p]
$NH + NH_3, NH_3(v) + M \rightarrow N_2H_4 + M^m$	4×10^{-35}	[69][i]
$NH + NH_3 + NH_3 \rightarrow N_2H_4 + NH_3$	1×10^{-33}	[69]
$NH_2 + NH_2 + Ar \rightarrow N_2H_4 + Ar$	2.9×10^{-30}	[70]
$NH_2 + NH_2 + NH_3 \rightarrow N_2H_4 + NH_3$	6.9×10^{-30}	[46]

Table 1. Continued

Reaction	Rate coefficient	Reference
$N_2H_2 + NH_2 \rightarrow N_2 + H + NH_3$	$1.5 \times 10^{-13}\ (T_g/300)^{4.05}\ e^{810/T_g}$	[62]
$N_2H_3 + H \rightarrow NH_2 + NH_2$	2.7×10^{-12}	[71]
$N_2H_3 + N_2H_3 \rightarrow NH_3 + NH_3 + N_2$	5×10^{-12}	[72]
$N_2H_3 + N_2H_3 \rightarrow N_2H_4 + N_2H_2$	2×10^{-11}	[73]
$N_2H_4 + N \rightarrow N_2H_2 + NH_2$	1.3×10^{-13}	[71]
$N_2H_4 + H \rightarrow N_2H_3 + H_2$	$1.2 \times 10^{-11} e^{-1260/T_g}$	[74]
$N_2H_4 + NH_2 \rightarrow NH_3 + N_2H_3$	5.2×10^{-13}	[71]

[a] Rate constant in $cm^3\ s^{-1}$ for 2-body reactions and $cm^6\ s^{-1}$ for 3-body reactions. For radiation reactions, units are in s^{-1}.
[b] Rate constant calculated by using cross-section data from the indicated reference.
[c] Superelastic collision cross-section calculated using detailed balance.
[d] Cross-section is the same as the reaction for the ground state, with the threshold shifted by the excitation threshold of $NH_3(v)$.
[e] Cross-section estimated by shifting and scaling the ground state cross-section by the excitation threshold.
[f] Estimated to have the same cross-section as NH_3.
[g] Reaction is included for energy loss, but the excited state is not tracked.
[h] Rate constant estimated by analogy.
[i] M is all major neutral species unless otherwise specified.
[j] M is one of NH_3, $NH_3(v)$, NH_2 or NH.
[k] Estimated.
[l] M is one of N^+, NH^+, NH_2^+, NH_3^+, NH_4^+. In the case of NH_4^+, the products are NH_3 and H_2.
[m] M is one of Ar, H, or H_2.
[n] M is one of N^+, NH^+, NH_2^+ or NH_3^+.
[o] Trapped rate for the radiation reaction.
[p] M is one of N, H, H_2, N_2, NH_3, $NH_3(v)$.

has a small rate coefficient, the total rate of the reaction can be large as the pressure increases. As the temperature increases, other endothermic reactions also begin to become important. One such process is the abstraction of H from NH_2 and NH_3 by H atoms, directly producing H_2:

$$H + NH_2 \rightarrow H_2 + NH \qquad (k = 1.1 \times 10^{-11}\ cm^3\ s^{-1} \text{ at } 2000\,K), \tag{6a}$$

$$H + NH_3 \rightarrow H_2 + NH_2 \qquad (k = 5.0 \times 10^{-14}\ cm^3\ s^{-1} \text{ at } 2000\,K). \tag{6b}$$

In the afterglow and downstream of the discharge region, neutral chemistry is most important. At this time the bulk of the dissociated NH_3 is in the form of N, H and NH_2. At pressures of $\geqslant$100 Torr and as the gas cools, 3-body reactions begin to dominate the mechanism. A large fraction of H_2 is formed downstream by 3-body association reactions. For example, the reactions:

$$H + H + Ar \rightarrow H_2 + Ar \qquad (k = 2.1 \times 10^{-30} T_g^{-1}\ cm^6\ s^{-1}), \tag{7a}$$

$$H + H + NH_3 \rightarrow H_2 + NH_3 \qquad (k = 1.4 \times 10^{-31}\ cm^6\ s^{-1}) \tag{7b}$$

produce H_2 within a few ms at pressures $\geqslant$100 Torr. The fractional contribution from these (and similar) processes

depends on the mole fractions of the third body and the fractional dissociation of the NH_3.

Loss of H by 3-body reassociation with NH_2 to form NH_3 can be important as the rate coefficient for this reaction is large, particularly with NH_3 as the third body ($k = 6.0 \times 10^{-30}\,cm^6\,s^{-1}$). The loss of H by this mechanism is rate limited by the density of NH_2 which is typically not large. Formation of N_2H_x ($x = 2, 3, 4$) by 2- and 3-body reactions tends to deplete NH_2. The primary pathways for producing N_2H_x ($x = 2, 3, 4$) are

$$NH_2 + NH \rightarrow N_2H_2 + H \quad (k = 2.5 \times 10^{-9} T_g^{-0.5} cm^3\,s^{-1}), \tag{8a}$$

$$\rightarrow N_2H_3 \quad (k = 1.16 \times 10^{-10}\,cm^3\,s^{-1}), \tag{8b}$$

$$NH_2 + NH_2 + NH_3 \rightarrow N_2H_4 + NH_3 \quad (k = 6.9 \times 10^{-30}\,cm^6\,s^{-1}). \tag{8c}$$

Although NNH is potentially an important intermediate species, its density is typically low due to its high reactivity. The density of NNH was not explicitly included in the mechanism as its rate coefficient decomposition to N_2 and H is much faster than for production from N_2H_2:

$$N_2H_2 + H \rightarrow NNH + H_2 \quad (k = 1.4 \times 10^{-17}\, T_g^{2.63} e^{115/T_g}\, cm^3\,s^{-1}) \tag{9a}$$

$$NNH \rightarrow N_2 + H \qquad (k = 2.7 \times 10^{16} T_g^{-0.53} e^{-3404/T_g}\, s^{-1}) \tag{9b}$$

To simplify the reaction mechanism and to reduce the mathematical stiffness of the mechanism, the above reactions were combined to

$$N_2H_2 + H \rightarrow N_2 + H_2 + H \tag{10}$$

with the rate coefficient being that of the slower reaction, equation (9*a*).

The surface-to-volume ratio in microdischarges is high due to the small dimensions of the reactor and so the interaction of radicals with surfaces is potentially important. To this effect a simple surface reaction mechanism was included. Ions and excited states striking the surfaces were returned to the plasma with unit probability after being neutralized or quenched by the walls. The reaction of H on the walls to form H_2 can be important especially in low pressure discharges where 3-body recombination rates are small [16]. Jackson and Pearson [17] investigated the recombination of atomic hydrogen to yield H_2 on metallic surfaces such as Cu and W. They found reaction probabilities to be between 0.3 and 0.6 for Cu and ≈0.9 for W at incident energies < 1.5 eV. In this work, 10% (probability = 0.1) of H striking the surfaces was returned to the plasma as H_2 as a worst case scenario. The probability for H recombination on surfaces was varied in the model to determine the sensitivity of the results to our choice for this parameter. Increasing the probability for recombination from 0.1 to 0.5 increased the exit H_2 densities by not more than 7%.

4. Scaling of microdischarge production of H_2: plug flow modelling

To characterize the production of H_2 in microdischarges, the following parameters are used:

$$\eta = \frac{2}{3}\frac{[H_2]\, v_e A_e}{[NH_3] v_i A_i}, \tag{11a}$$

$$\gamma(H_2) = \frac{P}{[H_2] A_e v_e}, \tag{11b}$$

$$\gamma(NH_3) = \frac{P}{[NH_3] A_i v_i}, \tag{11c}$$

where $[H_2]$ and $[NH_3]$ are the densities of H_2 and NH_3 at the exit and inlet, respectively; and v_i and v_e are the inlet and exit speeds. A_e and A_i are the cross sectional areas at the exit and inlet of the reactor and P is the power deposition. η, the conversion efficiency, is the fraction of H entering the discharge in the form of NH_3 that exits in the form of H_2. $\gamma(H_2)$, the H_2 energy efficiency, is the energy required to produce an H_2 molecule at the exit. $\gamma(NH_3)$, the NH_3 energy deposition, is the energy deposited per inlet NH_3 molecule.

Fractional power dissipation by electron impact as a function of T_e in pure NH_3 discharges based on rate coefficients produced from solutions of Boltzmann's equation is shown in figure 2(*a*). At low T_e, most of the power is dissipated in vibrational excitation of NH_3 ($\Delta\varepsilon = 0.11$ eV). Power loss to momentum transfer is typically small (<1%) at low temperatures (<2 eV) and is negligible at higher T_e. Power dissipated in attachment to form H^- is also small (at most a few per cent). Fractional power dissipation into dissociative excitement forming NH_2 and H has a peak value of 0.7 at $T_e = 2.2$ eV. Production of NH and 2H has a peak fractional dissipation of 0.32 at T_e = 8.5 eV. Electron impact ionization to form NH_3^+ and NH_2^+ with thresholds of 10.2 and 16.0 eV, respectively, account for 10–20% of power dissipation for $T_e > 6$ eV. This is not unexpected. Based on solutions of Boltzmann's equation for the EED in pure NH_3, for T_e = 3.6 eV 10% of electrons have energies above 10.2 eV. For T_e = 5 eV, 25% of electrons have energies of about 10.2 eV. For moderate T_e (2–3 eV) the dominant form of power dissipation is by neutral dissociation of NH_3, whereas at higher T_e, ionization reactions are more important.

The effect of dilution of NH_3 by Ar on the fractional power dissipation by electron impact processes is shown in figure 2(*b*) for Ar/NH_3 = 90/10. For $T_e > 2.5$–3 eV, most of the power is dissipated in exciting and ionizing Ar. The fractional dissipation by dissociation of NH_3 into NH_2 + H is half that of pure NH_3 for $T_e < 2$ eV and this reaction is the dominant source of H production for this mixture. Excitation and ionization of Ar are not total losses with respect to H production as Penning and charge exchange reactions can recoup H atoms. The net energy efficiency of those processes is, however, smaller.

The rates of production of H as a function of T_e for Ar/NH_3 mixtures at 100 Torr are shown in figure 2(*c*). This rate is $[NH_3]\sum_i k_i n_i$, where k_i is the rate coefficient for the ith reaction and n_i is the number of H atoms produced. This value can be interpreted as the rate of production of H atoms per electron from a distribution having temperature T_e. As

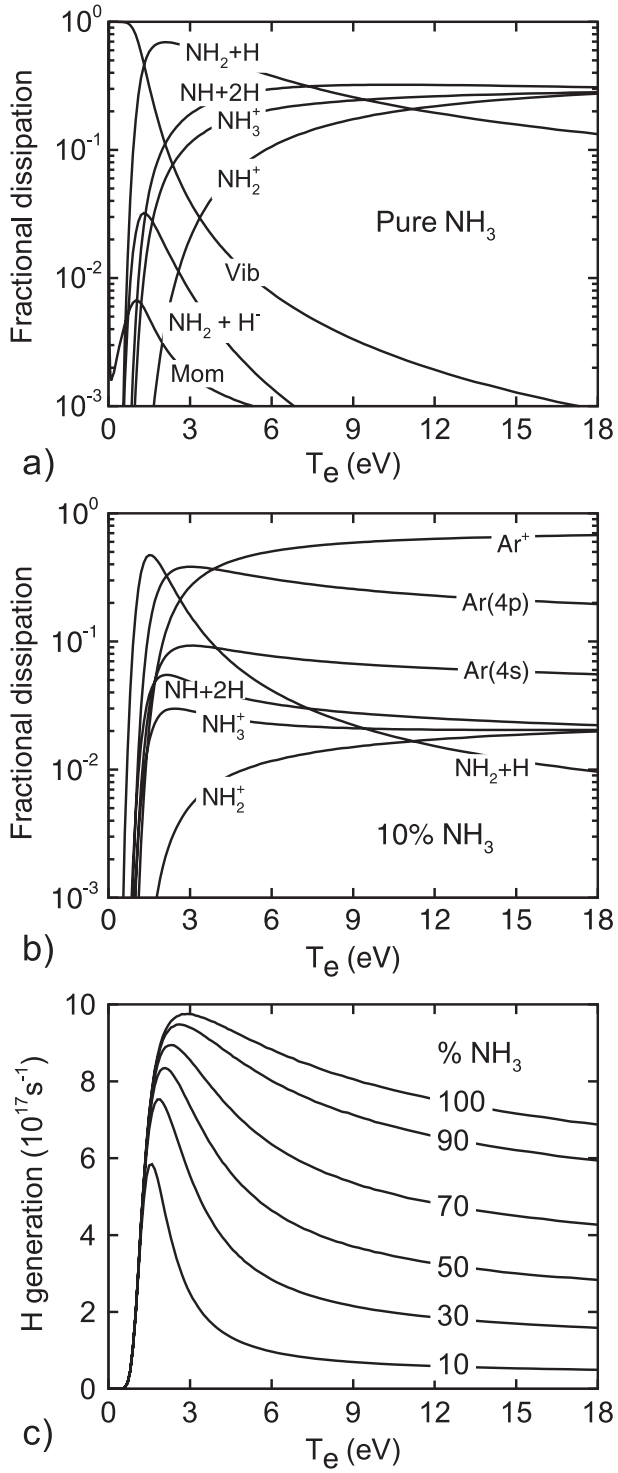

Figure 2. Discharge parameters obtained from electron impact rate coefficients as a function of electron temperature, T_e. (*a*) Fractional power deposition by electron impact in pure NH_3, (*b*) fractional power deposition in Ar/NH_3= 90/10 and (*c*) total H generation by electron impact on NH_3 per unit power for different NH_3 mole fractions. The optimum T_e for H generation is less than 3 eV.

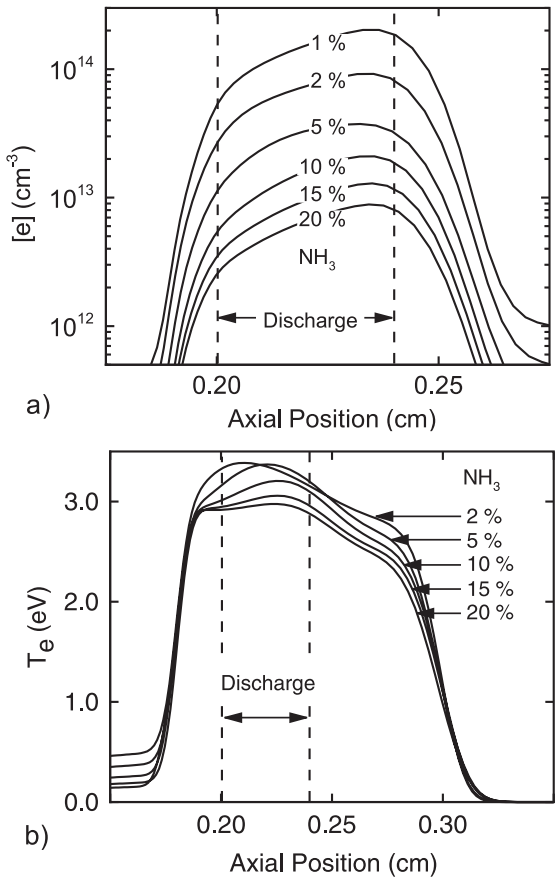

Figure 3. Plasma characteristics along the axis of the discharge with varying NH_3 mole fractions and constant flow speed of 10 m s^{-1}. (*a*) Electron density and (*b*) electron temperature. The electron density significantly increases with decreasing mole fraction while T_e changes little.

the NH_3 mole fraction decreases from 1 to 0.1, the optimum T_e for H atom production decreases from 3 to 1.6 eV and the peak production rates of H decrease from 9.7×10^{17} to 5.8×10^{17} s^{-1}. These estimates ignore the production of H by dissociative recombination of NH_3^+ and NH_2^+, which is not terribly important since production of H is generally dominated by neutral dissociation at low T_e. The presence of Ar shifts the optimum T_e for H production not only to a lower value but also into a narrower range of T_e due to the cut-off of the tail of the EED resulting from electronic excitation of Ar (11.6 eV). This effect could be mitigated by electron–electron collisions, which thermalizes the EED towards a Maxwellian at high fractional ionizations. These results do not necessarily imply that H production must decrease due to increasing dilution with Ar. This is because the electron density could increase (due to increase in ionizing reactions) at a higher rate than the reduction in NH_3 density. The results do, however, indicate that as the Ar mole fraction is increased, T_e should be lower to preferentially dissociate NH_3 rather than excite Ar. They also indicate that the optimum operating conditions lie in a narrower range of T_e and so operation of a device may need to be more carefully controlled.

The simplified geometry used for the plug flow modelling is shown in figure 1(*b*). The flow enters into a cylindrical tube 300 μm in diameter and 1 cm long. Power deposition is specified to occur over a 0.4 mm length (the discharge region). Using the plug flow model, the electron density (n_e) and T_e are shown in figure 3 as a function of NH_3 fraction for a pressure of 100 Torr, inlet flow speed of 10 m s^{-1} (corresponding to

5.6 sccm) and a power density 2.5 kW cm^{-3} (in the discharge region). The total power deposition is 0.1 W. Increasing the NH_3 mole fraction increases the power dissipation per electron by dissociative excitation (rather than ionization) and so, for fixed power deposition, the electron density decreases. From 1% to 20% NH_3, the electron density decreases by a factor of 20. (The reduction of electron density by dissociative attachment is small.) Note that n_e increases in traversing the discharge, a result of depletion of NH_3 and decrease in gas density due to gas heating. T_e did not show a marked difference in the range of NH_3 mole fractions considered. The increase in NH_3 mole fractions increases the rate of inelastic electron impact reactions having lower threshold energies and so lowers T_e. This fortuitously lowers T_e from an above optimum value (>3 eV) into a regime where H production is larger.

The densities of H and H_2 are shown in figure 4 along the axis of the discharge for different NH_3 fractions between 1% and 20% with a flow speed of 10 m s^{-1} (5.6 sccm). The density of H increases at the leading edge of the discharge as electron impact dissociation of NH_3 begins. At high NH_3 fractions, H densities peak at the edge of the discharge ((2–3) $\times$ 10^{16} cm^{-3}) before decreasing due to reassociation. At NH_3 mole fractions exceeding 10%, there is a rapid decrease in H atom density beginning immediately at the edge of the discharge region. This is due to the more rapid rate of recombination with NH_2 to form NH_3 and with H to form H_2 with NH_3 as the third body. (Recall that the 3-body rate coefficient for reassociation of H is larger with NH_3 as the third body compared with Ar.) With low mole fractions of NH_3 (<5–6%), the H atom density continues to increase downstream of the discharge (to (5–6) $\times$ 10^{16} cm^{-3}). This is in large part due to the cooling of the gas which increases the density of H atoms and the fact that with low mole fractions of NH_3, H is not rapidly consumed by 3-body processes (e.g. recombination with NH_2 and NH_3) that would otherwise decrease its density.

H_2 production, shown in figure 4(*b*) increases with increasing NH_3 mole fraction but saturates at densities of (5–6) $\times$ 10^{16} cm^{-3} with NH_3 mole fractions of $\geqslant$10%. This trend results from at least two factors. The first is that there is a decrease in n_e as the fraction of NH_3 increases (as shown in figure 3(*a*)). This decrease in n_e offsets the increase in the rate of production of H atoms per electron obtained when increasing the NH_3 mole fraction (as shown in figure 2(*c*)). The second factor is based on energy utilization. For a fixed power deposition, as the NH_3 mole fraction increases, the fractional energy deposition into NH_3, β, increases, as shown in figure 4(*c*). β is large for low T_e (<2 eV) for all NH_3 mole fractions above 10% but this energy is largely expended in pathways that do not directly produce H atoms such as vibrational excitation. As T_e increases, the fraction of energy deposition expended in dissociative pathways increases but so does the energy deposition into argon. When T_e is large enough (>4–5 eV) that inelastic electronic excitation and ionization of both Ar and NH_3 are important, β increases directly with the NH_3 mole fraction. In the intermediate regime and for the range of T_e in the main part of the discharge (2.5–3 eV), the proportion of power deposition into NH_3 and its distribution into dissociative modes are sensitive functions of NH_3 mole fraction.

The density and flux of H_2 at the exit of the flow tube and η, the efficiency of H conversion, for various flow speeds (sccm

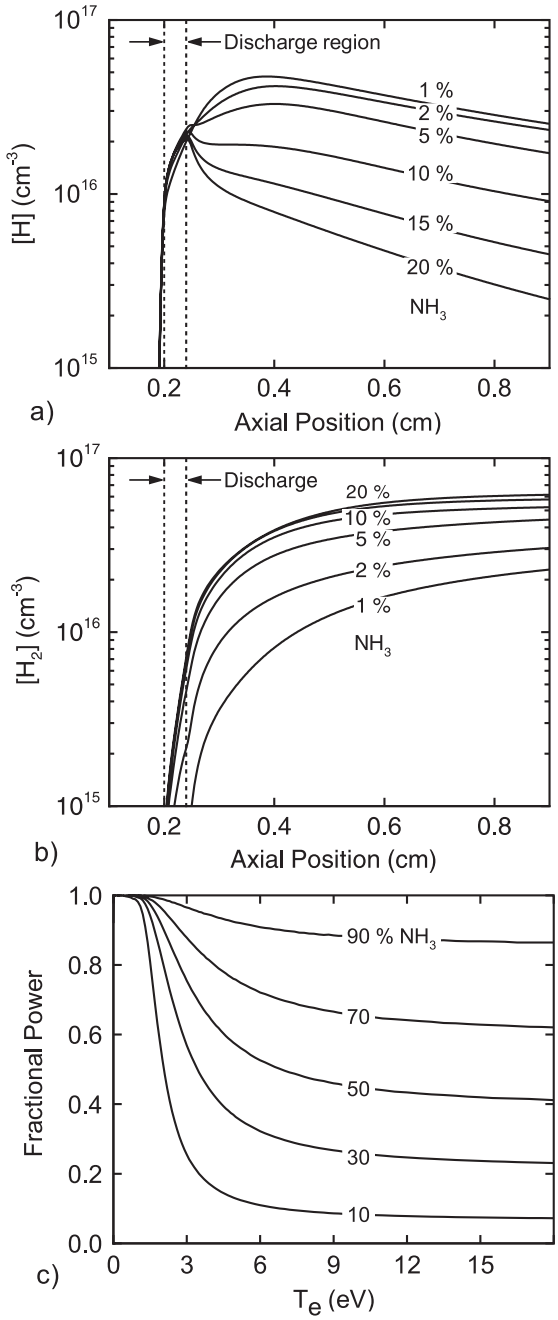

Figure 4. Plasma parameters while varying NH_3 mole fractions for a constant flow speed of 10 m s^{-1}. (*a*) H density, (*b*) H_2 density and (*c*) fractional power deposition into NH_3. H_2 production saturates for constant power deposition at mole fractions of 15–20%.

at the inlet) as a function of NH_3 mole fraction, are shown in figure 5. (Note that flow speed of 1 m s^{-1} corresponds to $\approx$0.56 sccm.) The H_2 density, the efficiency of conversion of NH_3 to H_2, η, and the eV per H_2 molecule produced, $\gamma(H_2)$, are also shown as a function of eV per inlet NH_3 molecule, $\gamma(NH_3)$, in figure 6. The pressure was 100 Torr and the power in the discharge region was 2.5 kW cm^{-3} (total power 0.1 W).

At flow speeds of 2.5–40 m s^{-1} (1.4–22.4 sccm) the time spent in the discharge region ranged from 160 to 10 μs. For a fixed inlet mole fraction of NH_3, low flow rates result in larger $\gamma(NH_3)$ and so produce larger rates of dissociation.

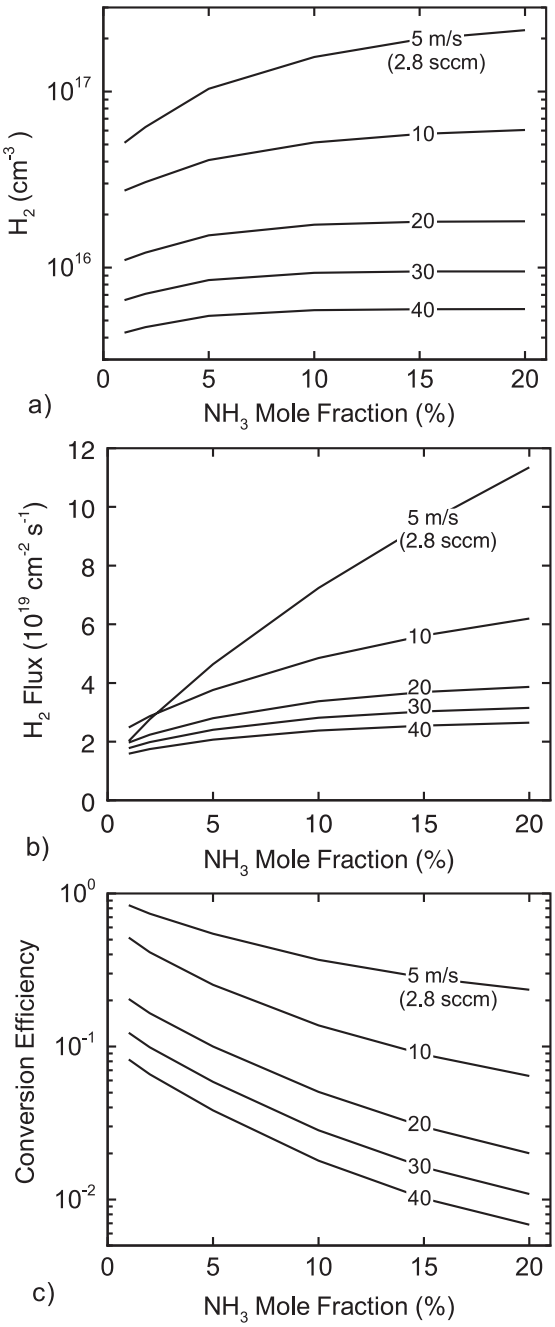

Figure 5. Hydrogen production at the exit of the reactor as a function of NH_3 mole fraction and flow speed. (*a*) H_2 density, (*b*) H_2 flux and (*c*) η, hydrogen conversion efficiency. Conversion efficiencies generally increase in parameter spaces which produce a small net flux of H_2.

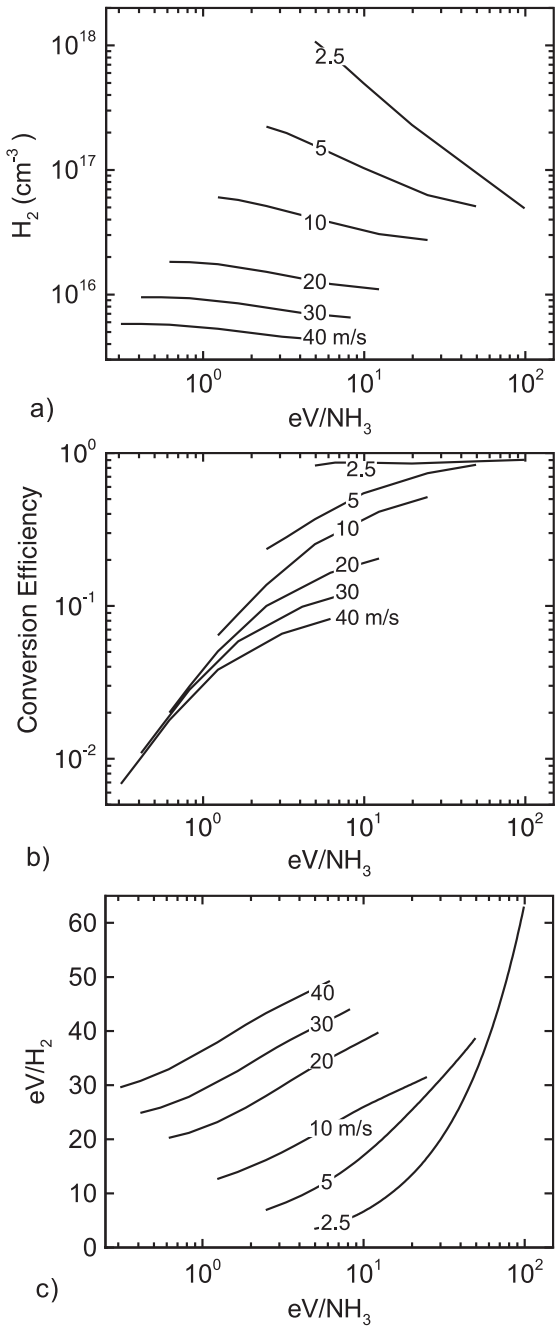

Figure 6. Hydrogen production at the exit of the reactor as a function of NH_3 energy deposition efficiency, $\gamma(NH_3)$, and flow speed. (*a*) H_2 density, (*b*) η, hydrogen conversion efficiency, and (*c*) $\gamma(H_2)$, hydrogen power efficiency. Power efficiency (lower is better) typically optimizes at low eV/NH_3 where conversion efficiency is low.

Larger densities and fluxes of H_2 at the exit are therefore produced. At high flow rates, the residence time of NH_3 in the discharge region is short enough (and $\gamma(NH_3)$ low enough) that there is no significant fractional dissociation of the NH_3. As the flow rate decreases and $\gamma(NH_3)$ increases, there is significant fractional dissociation and so there is an advantage to increasing the NH_3 mole fraction to capture more energy into dissociative modes. A secondary effect of the increase in fractional dissociation is the increase in flow speeds to maintain a constant pressure.

Conversion efficiencies generally decrease with increasing flow rate and mole fraction. Maximum conversion efficiencies are obtained when dissociation rates are large, which occurs when $\gamma(NH_3)$ is large, which in turn occurs when the NH_3 mole fraction and inlet speed (sccm) are both low. These conditions unfortunately do not produce a high H_2 output flux. Conversely, although the efficiency of conversion is low for higher NH_3 mole fractions, the outlet flux of H_2 is higher.

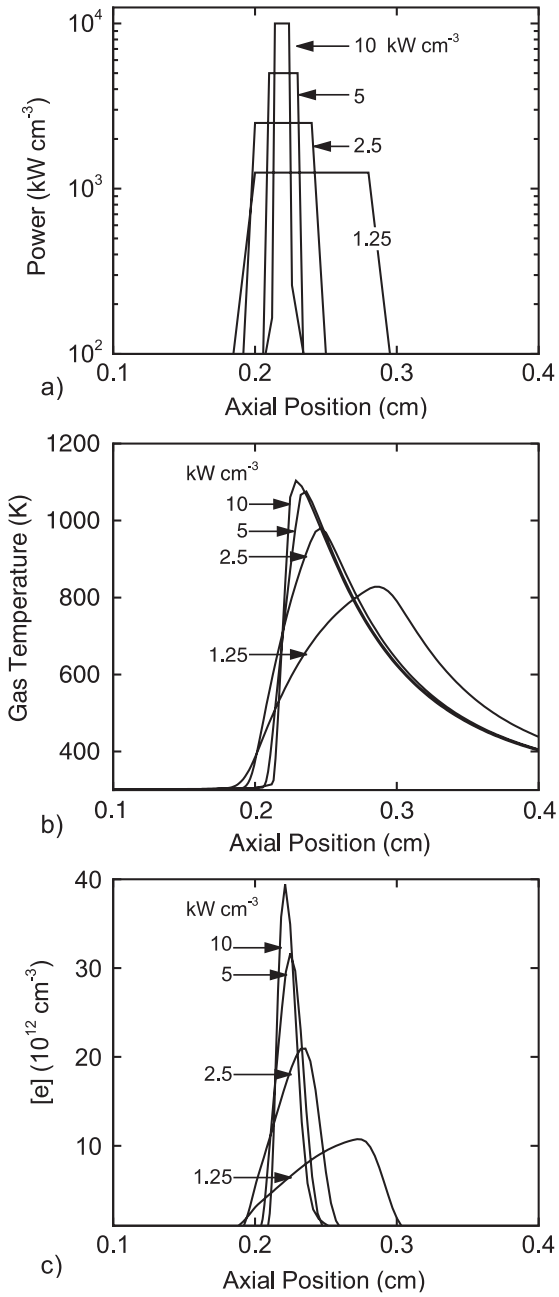

Figure 7. Plasma parameters along the axis for constant total power deposition (0.1 W) while varying the peak power deposition. (*a*) Specified power deposition, (*b*) gas temperature and (*c*) electron density. High specific power deposition produces locally high gas temperatures and electron densities.

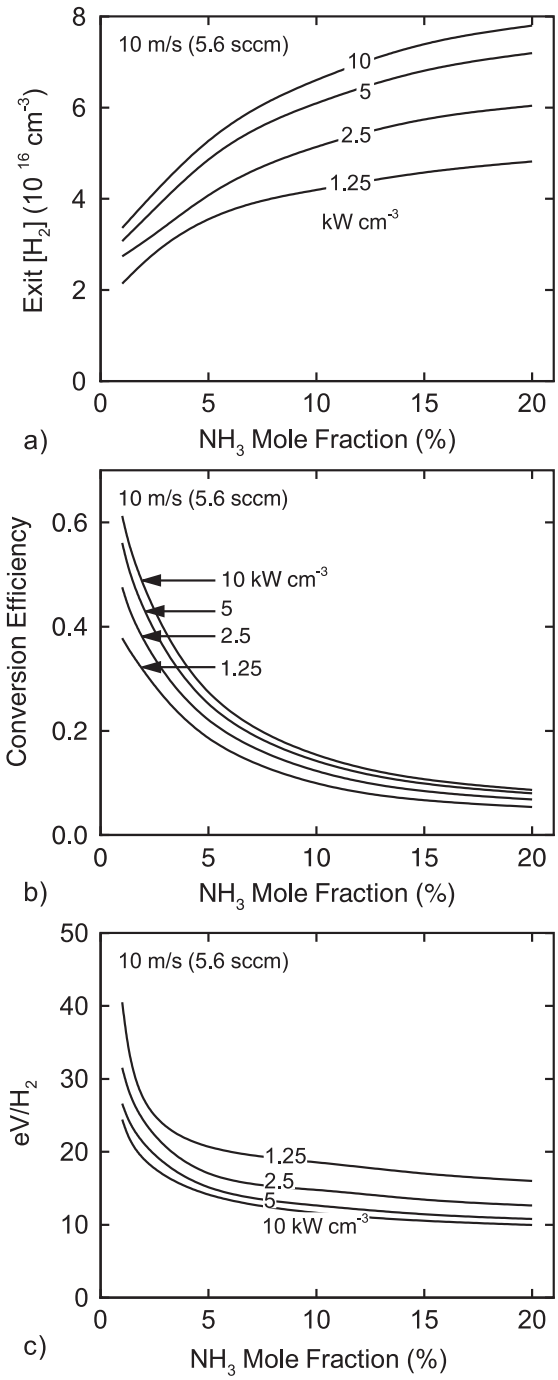

Figure 8. Plasma parameters as a function of NH_3 mole fraction for constant total power (0.1 W) while varying the peak power deposition. (*a*) H_2 density, (*b*) η, hydrogen conversion efficiency and (*c*) $\gamma(H_2)$, hydrogen power efficiency. H_2 and conversion efficiency are favoured by high specific power.

From an application standpoint, there is a tradeoff between conversion of NH_3 to H_2 (fuel utilization) and net output flux of H_2. A measure of the latter is the energy required to produce an H_2 molecule, $\gamma(H_2)$, which is important because the maximum energy recovered from a H_2 molecule in a fuel cell is 2.5 eV. This tradeoff is shown in figure 6(*c*), where, $\gamma(H_2)$ is shown as a function of energy deposition per feedstock NH_3, $\gamma(NH_3)$. For a constant power deposition, $\gamma(NH_3)$ decreases with increasing mole fraction (energy distributed over more NH_3 molecules) or increase in inlet speed (smaller residence time). At high flow speeds, $\gamma(H_2)$ is too large (few 10s eV) to be useful in producing feedstock for a fuel cell. At the lowest flow speed (2.5 m s^{-1}) and highest NH_3 mole fraction (20%) investigated, $\gamma(H_2)$ was 3.3 eV per H_2 created and η was 0.9, values that begin to become interesting for local H_2 production. Further reduction in flow speed to 1.25 m s^{-1} (not shown in the figure) caused a reduction in H_2 flux and increase in $\gamma(H_2)$. At a flow speed of 2.5 m s^{-1}, the conversion efficiency, η, was high (0.8–0.9) for all mole

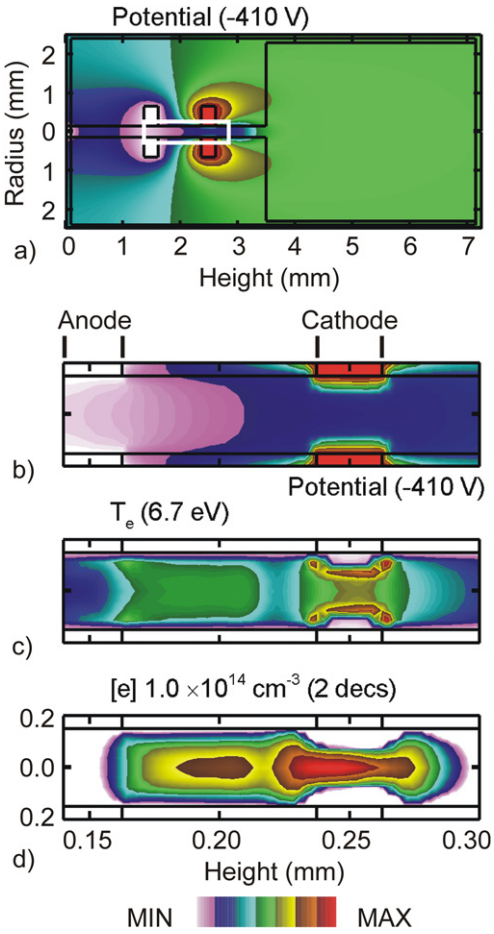

Figure 9. Base case plasma characteristics for the 2D model for a power deposition of 1 W, Ar/NH_3 = 90/10 and a flow rate of 10 sccm (≈18 m s^{-1}). (*a*) Plasma potential for the entire reactor, (*b*) plasma potential in the enlarged region designated by the white outline above, (*c*) electron temperature and (*d*) electron density. The scales are linear except for electron density that is plotted on a 2-decade log scale.

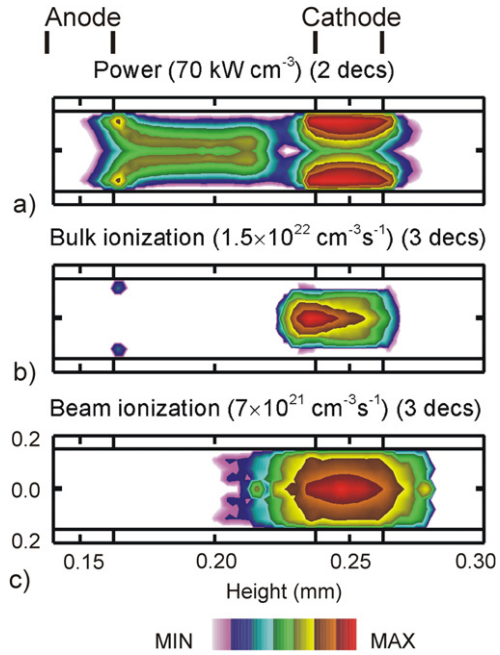

Figure 10. Power deposition and ionization sources for the base case: (*a*) power density (2-decade log scale), (*b*) ionization by bulk electrons (3-decades) and (*c*) ionization by beam electrons (3-decades). Ionization is nearly equally shared between bulk and beam electrons.

fractions, implying that the H_2 density was unlikely to improve significantly at flow speeds lower than 2.5 m s^{-1}. Lower flow speeds result in sufficiently long residence times that power was expended in dissociating the product H_2. As a result, the reduction of $\gamma(H_2)$ to lower than 3.3 would require optimizing other parameters in the system. Most such parameters have to do with more efficiently utilizing the thermal energy of the discharge to dissociate the NH_3. Once the discharge energy is expended to heat the gas, utilizing that heat to further thermally dissociate the feedstock gas can only improve efficiency. For a given total power deposition, increasing the power density will increase the local gas temperature. Since thermal dissociation has an exponential temperature dependence, more dissociation will likely be obtained even though the volume is smaller. This strategy is discussed below. Another strategy is to thermally engineer the device to minimize heat transfer out of the discharge and so reduce cooling rates.

The consequences of varying power density (kW cm^{-3}) while keeping total power constant (0.1 W) on plasma characteristics are shown in figure 7. The pressure was 100 Torr, the NH_3 mole fraction was 0.1 and the inlet flow speed was 10 m s^{-1} (5.6 sccm). The axial power densities, shown in figure 7(*a*), maintain the total energy deposition per unit volume a constant for a given flow rate. The maximum T_g (shown in figure 7(*b*)) increased from 800 to 1100 K as the power density was increased from 1.25 to 10 kW cm^{-3}. The maximum value of n_e (shown in figure 7(*c*)) increased nearly linearly from 1.0×10^{13} cm^{-3} to 3.8×10^{13} cm^{-3} as the power density was increased from 1.25 to 10 kW cm^{-3}.

If H_2 production was purely a function of energy deposition, then its value would be independent of the variation in the spatial distribution of power deposition examined here. We found that not to be the case. For example, the density of H_2 and the conversion efficiency η at the exit as a function of NH_3 mole fraction are shown in figure 8 for different power densities and constant total energy deposition. In principle, η should be independent of power density. The H_2 densities (figure 8(*a*)) increased with increasing power densities and the effect was more pronounced at higher NH_3 mole fractions. At higher power densities, T_g increases thereby increasing the contribution of thermal decomposition of NH_3 to the production of H atoms and other endothermic processes such as H abstraction. As a result, η increased with increasing power deposition (as shown in figure 8(*b*)) while $\gamma(H_2)$ was reduced by nearly 60% by increasing the power density from 1.25 to 10 kW cm^{-3} (as shown in figure 8(*c*)).

5. Scaling of microdischarge production of H_2: 2D modelling

Results from the plug flow model provide trends and scaling but are not able to accurately capture the consequences of spatial variations in, for example, power deposition or the emission of secondary electrons from the cathode. To provide

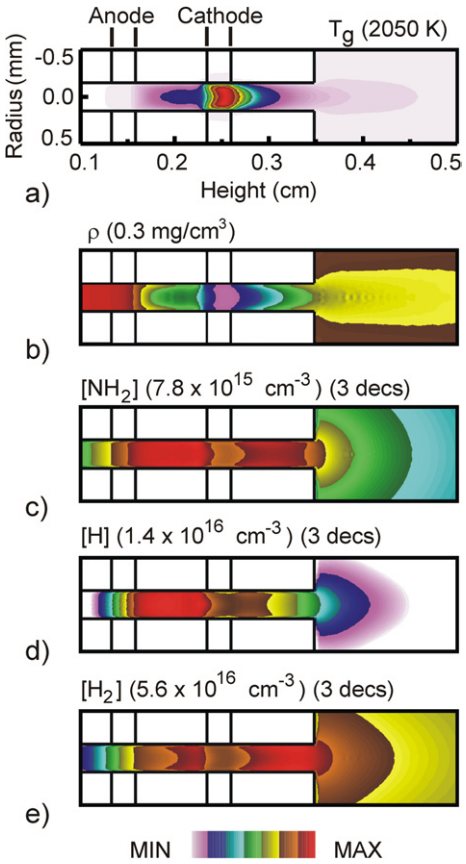

Figure 11. Neutral flow properties in the discharge region for the base case. (*a*) Gas temperature, (*b*) gas mass density, (*c*) NH_2 density, (*d*) H density and (*e*) H_2 density. Rarefaction of the gas by gas heating reduces densities of species in the hollow cathode.

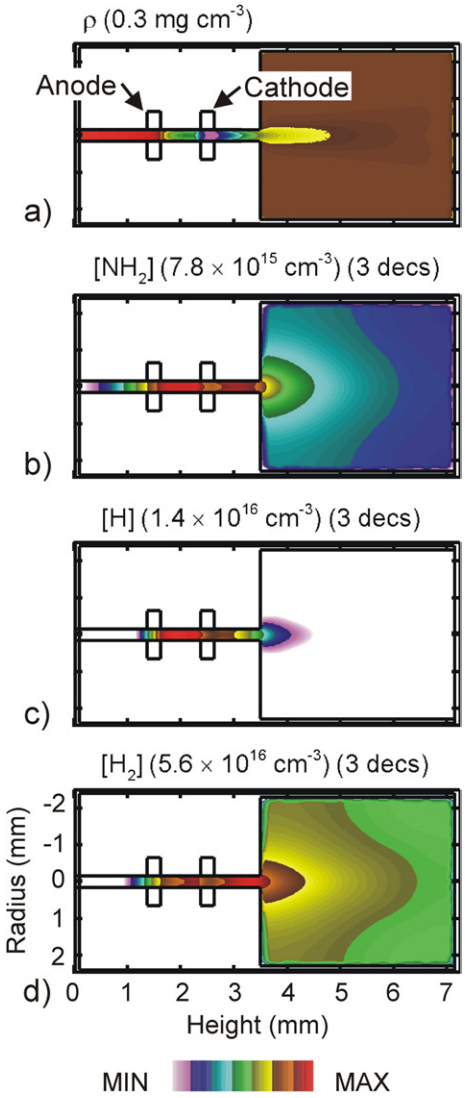

Figure 12. Neutral flow properties for the entire reactor. (*a*) Gas density, (*b*) NH_2 density, (*c*) H density and (*d*) H_2 density. Product densities decrease downstream as the plume expands.

insights into the consequences of spatial variations in plasma and flow properties, we used our two-dimensional model to investigate microdischarges within a similar parameter space as that for the plug flow modelling. The pressure and power for all the results reported in this section are 100 Torr and 1 W, respectively.

The geometry used for this study is shown in figure 1(*a*) and was discussed previously. In analogy to the plug flow model, the discharge region is between the centres of the electrodes (0.15–0.25 cm along the vertical axis). The electrons and the ions were initialized to have small densities (10^9 cm^{-3}) in a Gaussian distribution of width 200 μm in the centre of the reactor adjacent to the cathode. The velocity and density of the gas at the inlet was set based on the specified flow rate and the pressure. T_g was initialized to 300 K throughout the domain. The outlets were sufficiently far away from the discharge region that the normal gradients (along the flow direction) of flow quantities were assumed to be zero. A no-slip condition was imposed on all other surfaces in contact with the plasma.

The plasma potential, T_e and n_e for the base case (10 sccm, $Ar/NH_3 = 95/5$) are shown in figure 9. Power deposition and ionization sources are shown in figure 10. The steep gradients of the plasma potential near the cathode represent the cathode fall. The potential drop across the cathode fall is −330 V over a 100 μm distance producing an average electric field of 3.3 kV cm^{-1}. Ionization occurs from collisions of bulk electrons and the secondary beam electrons produced at the cathode as a result of ion bombardment. The maximum value of ionization from these two sources are within a factor of two (1.5×10^{22} cm^{-3} s^{-1} for bulk ionization and 7×10^{21} cm^{-3} s^{-1} for beam ionization). The plasma is segmented into a portion that appears hollow cathode-like (that is, dominantly negative glow) within the ring cathode and a portion that is positive column-like, extending along the axis towards the anode.

The ionization by beam electrons in the negative glow region contributes towards producing a local maximum in electron density of 1.1×10^{14} cm^{-3}. Ionization by bulk electrons is also a maximum in this region. As such, the vast majority of the power expended by electrons in the positive column portion of the discharge goes into non-ionizing dissociation reactions. Power deposition is dominated by ion acceleration and secondary electron emission within the hollow cathode and by conventional resistive heating in the positive column.

The gas temperature and densities of the neutral fluid, NH_2, H and H_2 are shown in figure 11. The densities of the

neutral fluid, NH_2, H and H_2 as they convect out of the reactor channel are shown in figure 12. T_g increases from 300 K at the inlet to 2050 K in the discharge region. The skew in the high temperature region to the right represents the convection of the gas by the flow. This peak in gas temperature is likely a lower limit as the boundary condition for the material temperatures was 300 K, which may artificially constrain the maximum T_g by having high rates of thermal conduction to the walls. Rarefaction of the gas occurs due to gas heating and reduces the fluid density within the cathode ring. This reduction in gas density lengthens the range of beam electrons emitted from the cathode and contributes to the hollow-cathode-like behaviour. On the other hand, the reduction in density reduces the density of collision partners for the electron and heavy particles, resulting in plasma chemistry occurring dominantly in the positive column region of the discharge. The rates of formation of NH_2 and H by electron impact have a maximum in the positive column portion of the plasma where T_e, at 3 eV, is close to the value that optimizes energy dissipation by dissociative excitation of NH_3. The production of H_2 is maximum in the hottest regions within the cathode due to abstraction of H from NH_2 (equation (6*a*)) and from NH_3 (equation (6*b*)) to a smaller degree. The contribution to H production from direct decomposition of NH_3 is not more than a few per cent of the total.

Downstream of the discharge, densities increase due to cooling of the gas. The H_2 production in the afterglow is dominated by volumetric 3-body recombination with a small contribution (<10%) from wall recombination. The recombination of H and NH_2 with NH_3 as the third body to form NH_3 ($k = 6 \times 10^{-30}\,cm^6\,s^{-1}$) competes with that of H_2 production (equation (7*b*), $k = 1.4 \times 10^{-31}\,cm^6\,s^{-1}$). The fraction of NH_3 production to H_2 production by these 3-body reactions is determined by the product of the ratio of the rate constants (≈40) and $[NH_2]/[H]$. While this can be a large fraction (≈90% in this case), the amount of H in this region is already <10 % of the H in the discharge region and hence the loss of H is not alarmingly large.

The conversion of NH_2 into N_2H_4 (equation (8*c*)) can also consume NH_2 when NH_2 densities are comparable to those of H. This is, in principle, advantageous because it eliminates a channel for H consumption, reassociation of H with NH_2 to reform NH_3. It is disadvantageous because the reservoir of H in NH_2 is made that much more distant from H_2 formation. These tradeoffs place a large premium on fully dissociating the NH_2 and NH fragments of NH_3 to minimize the reassociation reactions. Downstream of the plasma channel, the densities of all product species decrease in the expanding plume. However, the more rapid decrease in the H atom density indicates its consumption in reassociation reactions.

The densities of selected ions and neutral species along the axis of the 2D reactor are shown in figure 13. Ion densities extended significantly further upstream and downstream than shown in the plug flow model due to ambipolar diffusion (upstream) and convection (downstream). In the positive column region NH_4^+ is the most abundant ion as predicted by the global model. The lower thresholds for ionization of NH_x compared with Ar preferentially produce their ions in the positive column where T_e is low. Within the hollow-cathode region, the major ion is Ar^+. This results from ionization

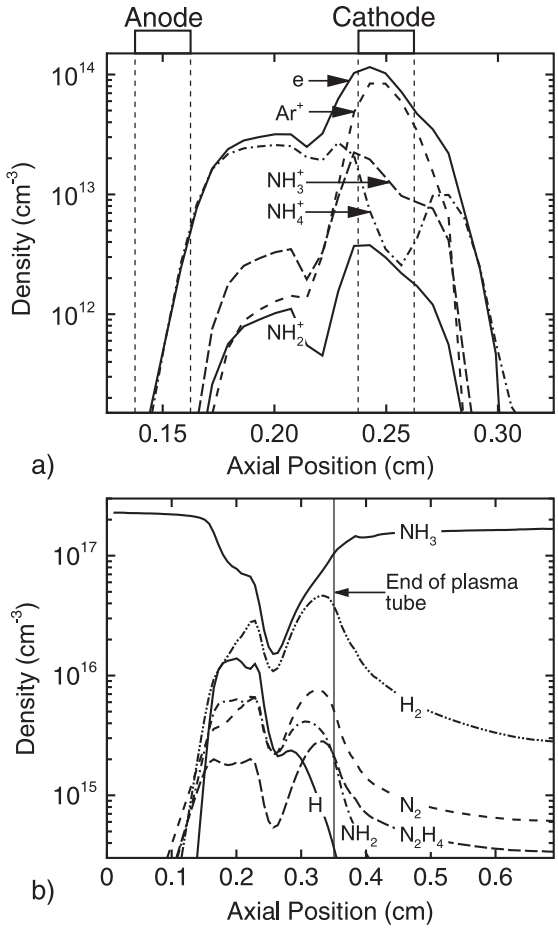

Figure 13. Densities of selected ions and neutral species along the axis of the discharge for the base case. (*a*) Charged species densities and (*b*) neutral species densities. Rarefaction and contributions from beam electrons result in Ar_+ having the largest ion density in the negative glow region.

being dominated by beam electrons which do not so clearly discriminate between species having differences in threshold energies of 5–10 eV. The low gas density in this region due to gas heating and the resulting lower rate of charge exchange reactions result in NH_3^+ being the dominant NH_x ion. Only downstream after gas densities rebound with cooling does charge exchange enable NH_4^+ to become the dominant ion again.

The dominant neutral species apart from NH_3 and Ar are H_2, N_2, N_2H_4, NH_2 and H. The reduction in densities of the H_2 and N_2 starting at the end of the plasma tube is due in large part to the expansion of the plume. These are stable end products and the gas temperature is not high enough in the downstream region for additional endothermic reactions to occur. The reduction in densities in the cathode region is due to gas heating. Note that the H_2 density decreased by a factor of only 2 in the cathode region even though the gas temperature increased by a factor of nearly 7 to 2050 K. This indicates a large source of H_2, which is H abstraction by H from NH_3 and NH_2 (equations (6*a*) and (6*b*)). Direct thermal decomposition of NH_3 plays a smaller role.

The densities and flow rates at the exit of the plasma tube will be used as the basis for commenting on efficiencies and

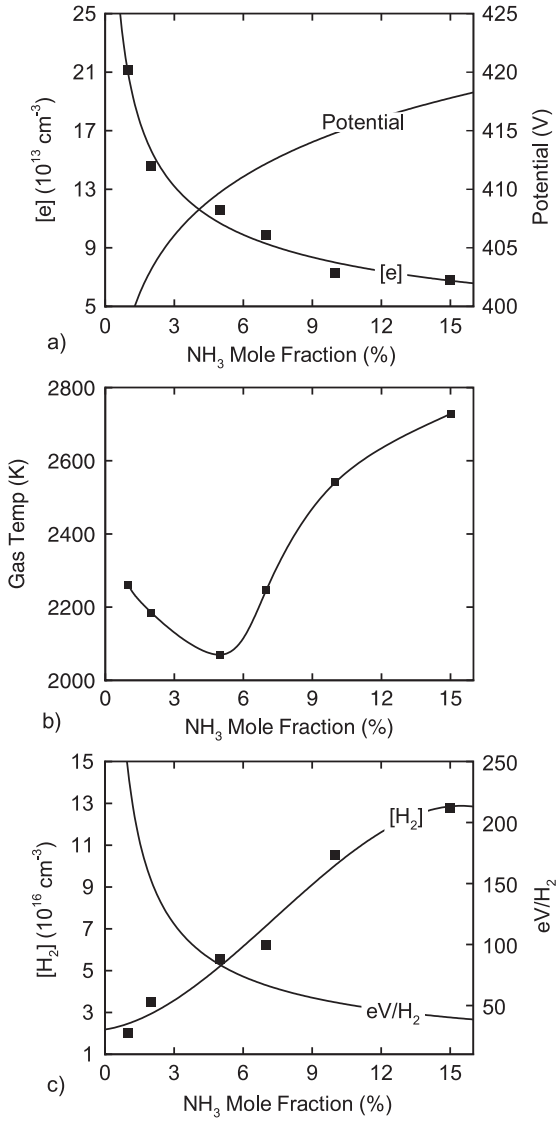

Figure 14. Variation of discharge and flow properties with NH_3 mole fraction for 1 W and 10 sccm (≈18 m s^{-1}). (*a*) Electron density and cathode voltage, (*b*) gas temperature and (*c*) H_2 density and $\gamma(H_2)$, hydrogen power efficiency.

conversion rates. The density of H_2 at the exit of the plasma tube is 4.6×10^{16} cm^{-3} and the efficiency of H conversion is $\eta = 0.41$ resulting in a total dissociation of NH_3 of 0.31. The rate of production of H_2 molecules is 1.6×10^{17} s^{-1} which for a power deposition of 1 W corresponds to $\gamma(H_2) = 39$ eV.

The consequences of NH_3 mole fraction on n_e, T_g and H_2 production are shown in figure 14. The values of n_e and T_g are on axis at the centre of the cathode and the values of [H_2] are at the end of the plasma tube. n_e decreases with increasing NH_3 mole fraction, as predicted by the plug flow model due to more rapid rates of power dissipation per electron. The plasma becomes more resistive when increasing the NH_3 mole fraction as indicated by the increase in voltage required to dissipate 1 W. The general trend is for T_g to increase with increasing NH_3 mole fraction. The sources of gas heating are largely Joule heating (including ion acceleration in the presheath and sheath) and dissociation reactions (Franck–Condon effects). At lower NH_3 mole fractions Joule heating from Ar^+ near the cathode was the primary source of gas heating, whereas, at higher NH_3 mole fractions, the dissociation of NH_3 and Franck–Condon relaxation provided the major source of heating. The exit [H_2] increased from 2.3 to 12.8 × 10^{16} cm^{-3} when increasing the NH_3 mole fraction from 1% to 15% for the same power deposition. This resulted in $\gamma(H_2)$ decreasing from 242 to 38. These trends are in-line with predictions from the plug flow model.

6. Concluding remarks

The production of H_2 in microdischarges sustained in Ar/NH_3 mixtures was computationally investigated using plug flow and two-dimensional models. Results from both models suggest that high conversion rates of NH_3 to H_2 occur at low NH_3 mole fractions and low flow speeds (or high residence times) both of which maximize the eV/NH_3 molecule deposited, $\gamma(NH_3)$. The T_e which maximizes the fraction of power dissipated in electron impact dissociation is ≈3 eV for pure NH_3 and <1.6 eV for Ar/NH_3 = 90/10. For constant power, an increase in NH_3 mole fraction reduced the electron density and produced a more resistive plasma. The H conversion efficiency η also decreased though that efficiency could be recovered by increasing power to increase $\gamma(NH_3)$. Results from the plug flow model also suggest that higher power densities in the discharge (for a given total power) can lead to more efficient production of H_2.

Acknowledgment

This work was supported by the National Science Foundation (CTS-0520368).

References

[1] Barbir F and Gómez T 1997 *Int. J. Hydrogen Eng.* **22** 1027
[2] Klemberg-Sapieha J E, Küttel O M, Martinu L and Wertheimer M R 1991 *J. Vac. Sci. Technol.* A **9** 2975
[3] Losurdo M, Capezzuto P, Bruno G and Irene E A 1998 *Phys. Rev.* B **58** 878
[4] van den Oever P J *et al* 2005 *J. Appl. Phys.* **98** 093301
[5] van den Oever P J *et al* 2006 *Plasma Sources Sci. Technol.* **15** 546
[6] Qiu H, Martus K, Lee W Y and Becker K 2004 *Int. J. Mass Spectrom.* **233** 19
[7] Hsu D D and Graves D B 2005 *Plasma Chem. Plasma Process.* **25** 1
[8] Fateev A *et al* 2005 *Plasma Process. Polym.* **2** 193
[9] Miller G P and Baird J K 1993 *J. Phys. Chem.* **97** 10984
[10] Dorai R and Kushner M J 2003 *J. Phys. D: Appl. Phys.* **36** 666
[11] Stafford D S and Kushner M J 2005 *J. Appl. Phys.* **98** 073303
[12] Lay B, Moss R S, Rauf S and Kushner M J 2003 *Plasma Sources Sci. Technol.* **12** 8
[13] Kushner M J 2004 *J. Appl. Phys.* **95** 846
[14] Arakoni R A, Stafford D S, Babaeva N Y and Kushner M J 2005 *J. Appl. Phys.* **98** 073304
[15] Bhoj A N and Kushner M J 2004 *J. Phys. D: Appl. Phys.* **37** 2510
[16] Vankan P, Engeln R and Schram D C 2005 *Appl. Phys. Lett.* **86** 101501
[17] Jackson B and Pearson M 1992 *J. Chem. Phys.* **96** 2378
[18] Hayashi M 1991 *Report No.* IPPJ-AM-19, Nagoya Institute of Technology
[19] Tachibana K 1986 *Phys. Rev.* A **34** 1007

[20] Rapp D and Englander-Golden P 1965 *J. Chem. Phys.* **43** 1464
[21] Zapesochnyi I P and Shimon L L 1966 *Opt. Spectrosc.* **11** 155
[22] McFarland R H and Kinney J D 1965 *Phys. Rev.* A **137** 1058
[23] Vriens L 1964 *Phys. Lett.* **8** 260
[24] Kannari F, Suda A, Obara M and Fujioka T 1983 *IEEE. J. Quantum Electron.* **QE-19** 1587
[25] Biondi M A 1976 *Principles of Laser Plasmas* (New York: Wiley)
[26] Hayashi M 1990 Electron collision cross-sections determined from beam and swarm data by Boltzmann analysis *Non-equilibrium Processes in Partially Ionized Gases* ed M Captielli and J Norman Bardsley (New York: Plenum)
[27] Märk T D and Dunn G H 1985 *Electron Impact Ionization* (Vienna: Springer)
[28] Tarnovsky V, Deutsch H and Becker K 1997 *Int. J. Mass. Spectrom. Ion Process.* **167–168** 69
[29] Geltman S 1973 *Quant J. Spectrosc. Radiat. Transfer* **13** 601
[30] Henry R J W, Burke P G and Sinfailam A-L 1969 *Phys. Rev.* **178** 218
[31] Smith A C H 1962 *Phys. Rev.* **127** 1647
[32] Itikawa Y *et al* 1986 *J. Phys. Chem. Ref. Data* **15** 985
[33] Phelps A V and Pitchford L C 1985 *Phys. Rev.* **31** 2932
[34] Banks P 1966 *Planet. Space Sci.* **14** 1085
[35] Janev R K, Langer W d, Evans D Jr. and Post D E 1987 *Elementary Processes in Hydrogen and Helium Containing Plasmas* (Berlin: Springer)
[36] Hayashi M 1979 *J. Physique* **40** C7/45-46
[37] Corrigan S J B 1965 *J. Chem. Phys.* **43** 4381
[38] Chan C F 1983 Reaction cross sections and rate coefficients related to production of positive ions *Lawrence Berkeley Laboratory Report No* LBID-632
[39] Morgan W L 2000 *Adv. At. Mol. Opt. Phys.* **43** 79
[40] Florescu A I and Mitchell J B A 2006 *Phys. Rep.* **430** 277
[41] Öjekull J *et al* 2004 *J. Chem. Phys.* **120** 7391
[42] Mitchner M and Kruger C H Jr. 1992 *Partially Ionized Gases* (New York: Wiley)
[43] Ellis H W, Pai R Y, McDaniel E W, Mason E A and Viehland L A 1976 *At. Data Nucl. Data Tables* **17** 177
[44] Ikezoe Y, Matsuoka S, Takebe M and Viggiano A 1987 *Gas Phase Ion-Molecule Reaction Rate Constants Through 1986* (Tokyo, Japan: Ion Reaction Research Group of the Mass Spectroscopy Society of Japan)
[45] Holstein T 1951 *Phys. Rev.* **83** 1159
[46] Kushner M J 1992 *J. Appl. Phys.* **71** 4173
[47] Balamuta J, Golde M F and Ho Y 1983 *J. Chem. Phys.* **79** 2822
[48] Hanson R K and Salimian S 1984 Survey of rate constants in the N/H/O system *Combustion Chemistry* ed W C Gardiner (New York: Springer)
[49] Meyer E, Olschewski H A,Troe J and Wagner H Gg 1969 Investigation of N_2H_4 and H_2O_2 decomposition in low and high pressure shock waves *Proc. 12th Int. Symp. on Combustion (University of Poitiers, France)* pp 345–55
[50] Deppe J, Friedrichs G, Ibrahim A, Romming v and Wagner H Gg 1998 *Ber. Bunsenges. Phys. Chem.* **102** 1474
[51] Thielen K and Roth P 1986 *AIAA J.* **24** 1102
[52] Corchado J C and J. Espiona-Garcia 1997 *J. Chem. Phys.* **106** 4013
[53] Rohrig M and Wagner H G 1994 The reactions of NH($X^3\ \Sigma$) with the water gas components CO_2, H_2O and H_2 *Proc. 25th Int. Symp. on Combustion (University of California of Irvine)* pp 975–81
[54] Stothard N, Humpfer R and Grotheer H-H 1995 *Chem. Phys. Lett.* **240** 474
[55] Xu Z-F, Fang D-C and Fu X-Y 1998 *Int. J. Quant. Chem.* **70** 321
[56] Pagsberg P B, Eriksen J and Christensen H C 1979 *J. Phys. Chem.* **83** 582
[57] Hack W, Wagner H Gg and Zaspypkin A 1994 *Ber. Bunsenges. Phys. Chem.* **98** 156
[58] Meaburn G M and Gordon S 1968 *J. Phys. Chem.* **72** 1592
[59] Nicholas J E, Spiers A I and Matin N A 1986 *Plasma Chem. Plasma Process.* **6** 39
[60] Xu Z-F, Fang D-C and Fu X-Y 1997 *Chem. Phys. Lett.* **275** 386
[61] Davidson R F and Hanson R K 1990 *Int. J. Chem. Kinet.* **22** 843
[62] Linder D P, Duan X and Page M 1996 *J. Chem. Phys.* **104** 6298
[63] Teng L and Winkler C A 1973 *Can. J. Chem.* **51** 3771
[64] Baulch D L *et al* 1992 *J. Phys. Chem. Ref. Data* **21** 411
[65] Cohen N and Westberg K R 1983 *J. Phys. Chem. Ref. Data* **12** 531
[66] Petrishchev V A and Sapozhkov A Yu 1981 *Kinet. Catal.* **22** 771
[67] Emel'kin V A and Marusin V V 1978 *Kinet. Catal.* **19** 1118
[68] Yamashita T 1979 *J. Chem. Phys.* **70** 4248
[69] Zetsch C and Stuhl F 1981 *Ber. Bunsenges. Phys. Chem.* **85** 564
[70] Lozovskii V A, Nadtochenko V A, Sarkisov O M and Cheskis S G 1979 *Kinet. Catal.* **20** 918
[71] Gehring M, Hoyermann K, Wagner H Gg and Wolfrum J 1971 *Ber. Bunsenges. Phys. Chem.* **75** 1287
[72] Schiavello M and Volpi G G 1962 *J. Chem. Phys.* **37** 1510
[73] Stief L J 1970 *J. Chem. Phys.* **52** 4841
[74] Vaghjiani G L, 1995 *Int. J. Chem. Kinet.* **27** 777